

Deep-learning mitigation of foregrounds and beam effects in 21-cm intensity mapping using hybrid frequency differencing and PCA

Zitong Wang,¹ Feng Shi,^{1,*} Le Zhang,^{2,3} Yanming Liu,¹ Xiaoping Li,¹ Ming Jiang,⁴ and Xiaofan Ma¹

¹*School of Aerospace Science and Technology, Xidian University, Xi'an 710126, China*

²*School of Physics and Astronomy, Sun Yat-sen University,*

²*Daxue Road, Tangjia, Zhuhai, 519082, P.R. China*

³*CSST Science Center for the Guangdong-Hong Kong-Macau Greater Bay Area, Zhuhai 519082, P.R. China*

⁴*National Key Laboratory of Radar Signal Processing, Xidian University, Xi'an 710126, P.R. China*

(Dated: November 20, 2025)

21-cm intensity mapping (IM) is a powerful technique to probe the large-scale distribution of neutral hydrogen (HI) and extract cosmological information such as the baryon acoustic oscillation feature. A key challenge lies in recovering the faint HI signal from bright foregrounds and frequency-dependent beam effects, which can compromise traditional cleaning methods like principal component analysis (PCA) by removing part of the cosmological signal. Deep-learning approaches have recently been proposed to mitigate these effects by learning mappings between contaminated and true cosmological signals. Building upon our previous work [1] on the frequency-differencing (FD) method, this study extends the framework to systematically compare FD-based and PCA-based UNet reconstructions using realistic simulations that include foregrounds and beam convolution. We find that both approaches perform comparably without beam or with a Gaussian beam, but under a realistic cosine beam they systematically underestimate the large-scale cross-correlation power spectrum, particularly for $k < 0.1 \text{ h Mpc}^{-1}$. To address this limitation, we explore a hybrid approach in which the UNet is trained with two input channels, one constructed from FD and the other from PCA cleaning, allowing the network to simultaneously exploit the strengths of both inputs. This two-channel strategy achieves superior performance, maintaining the cross-correlation power spectrum close to unity on large scales under a cosine beam, improving by 5.8% relative to either FD-based or PCA-based UNet alone. These results demonstrate that providing complementary FD and PCA information to a single deep network is an effective route to robust HI reconstruction, laying the groundwork for precision BAO measurements with future low-redshift 21 cm IM surveys.

I. INTRODUCTION

The cosmic 21-cm line of neutral hydrogen (HI) has emerged as a powerful tracer of large-scale structure in the post-reionization Universe. In particular, 21-cm intensity mapping (IM) has been proposed as an efficient method to map the three-dimensional distribution of HI without resolving individual galaxies [2–5]. By measuring the aggregate 21-cm brightness temperature fluctuations across low angular resolution voxels, IM surveys can rapidly cover enormous cosmological volumes. This opens a promising avenue to probe key cosmological observables at low redshifts, notably baryon acoustic oscillations (BAO) as a standard ruler for cosmic expansion, redshift-space distortions (RSD) as a probe of structure growth, and the bias and abundance of HI as tracers of the underlying matter field. Low-redshift 21-cm surveys offer a novel and complementary probe of cosmology (e.g., [6–9]), analogous to optical galaxy redshift surveys but with the potential for far greater volume and efficiency.

Over the past decade, a large number of interferometric and single-dish radio telescopes are currently conducting, and will continue to carry out, 21-cm intensity-mapping observations, including CHIME (Canadian Hy-

drogen Intensity Mapping Experiment) [10, 11], Tianlai [12–15], BINGO (Baryon acoustic oscillations In Neutral Gas Observations) [16, 17], MeerKAT (the South African SKA Pathfinder) [18, 19], HIRAX (the Hydrogen Intensity and Real-time Analysis eXperiment) [20], and the SKA (Square Kilometre Array) [21]. A series of pioneering experiments have demonstrated the viability of 21-cm intensity mapping at low redshift. The first detections of cosmological 21-cm fluctuations were obtained through cross-correlation of Green Bank Telescope intensity maps with galaxy redshift surveys [22–24], followed by similar measurements using the Parkes telescope [25]. The CHIME achieved the first interferometric detection of the 21-cm signal, reporting a statistically significant cross-correlation with eBOSS tracers [10]. More recently, a pilot intensity mapping survey with the MeerKAT array has produced the first high-significance detection of post-reionization HI signal, measured via cross-correlation with the WiggleZ galaxy survey at $0.4 < z < 0.459$ [26]. This represents the first practical demonstration of the multi-dish autocorrelation intensity mapping technique for cosmology and an important step toward a direct measurement of the HI auto-power spectrum, with deep MeerKAT observations already beginning to place upper limits on this quantity [27]. These results mark the transition of low-redshift 21-cm cosmology from proof-of-concept studies toward statistically robust detections, establishing the groundwork for future measurements of

* fshi@xidian.edu.cn

cosmology.

However, directly recovering the cosmological 21-cm signal from intensity maps remains challenging because astrophysical foregrounds, dominated by Galactic synchrotron, free-free emission and extragalactic point sources, are about 4 orders of magnitude brighter than the HI signal [28–31]. Over the years, numerous signal-separation algorithms have been proposed to address this issue. These techniques are generally classified as either blind or non-blind, depending on whether prior knowledge of the signal, foreground, or instrumental noise is required in the separation process. A comprehensive review of current foreground mitigation methods can be found in [32]. Representative blind (or semi-blind) approaches include Principal Component Analysis (PCA) [33], Singular Value Decomposition (SVD) [34, 35], Independent Component Analysis (ICA) [36, 37], and Generalized Morphological Component Analysis (GMCA) [38], all of which exploit the spectral smoothness of foregrounds to isolate the rapidly varying cosmological component. In contrast, non-blind approaches such as the Generalized Needlet Internal Linear Combination (GNILC) [39, 40], Gaussian Process Regression (GPR) [36, 41], and the Karhunen–Lo  e Transform [42] incorporate additional statistical priors or external templates, achieving improved separation at the cost of model dependence. In addition, the Bayesian framework [43–46] enables joint inference of the 21-cm signal and foregrounds, incorporating prior knowledge and naturally accounting for correlations and uncertainties. This probabilistic approach allows robust separation of the faint cosmological signal from dominant foregrounds while consistently propagating errors.

Furthermore, the telescope’s primary beam introduces additional complexity: its intrinsic chromaticity smooths the sky differently across frequencies, imprinting artificial spectral structures that mimic genuine fluctuations (e.g., [47]). This beam–frequency coupling reduces the apparent smoothness of the foregrounds, couples angular and spectral modes, and increases the number of PCA modes that must be removed, thereby elevating the risk of losing part of the cosmological signal. Both over- and under-subtraction can bias power-spectrum measurements [48, 49], and consequently, most existing 21-cm analyses still depend on cross-correlations with external galaxy surveys for robust detection. These challenges highlight the need for improved mitigation strategies that integrate established linear filters such as PCA with advanced reconstruction techniques, enabling more reliable and bias-resistant recovery of the underlying HI signal.

Recent efforts have explored machine-learning approaches to improve signal recovery beyond traditional linear foreground removal (e.g., [1, 50–58]). The Deep21 framework [51] demonstrated that a three-dimensional UNet can recover the HI signal with significantly less bias than PCA, leading to improved power-spectrum reconstruction across a wide range of scales and reducing the level of signal loss typical of linear cleaning. Building

on this result, [53] investigated the impact of frequency-dependent primary beams and showed that applying a UNet after PCA cleaning can partially restore modes suppressed by aggressive mode subtraction and effectively mitigate beam-induced spectral distortions. More recently, frequency-differencing (FD) combined with deep learning has been proposed as a complementary strategy, where differencing adjacent frequency channels reduces the dynamic range of the input data and enables the network to focus on learning the residual foreground structures [1]. These studies together demonstrate that deep learning can recover cosmological information that would otherwise be lost and that it is emerging as a powerful complement to traditional cleaning techniques.

Despite these advances, key limitations remain that must be addressed before unbiased cosmological measurements become feasible. In particular, it is still unclear how FD-based approaches perform in the presence of realistic, frequency-dependent beams and how they compare systematically with established PCA-based cleaning under identical conditions. Moreover, while PCA robustly removes the bulk of smooth foreground modes, it risks excessive signal loss, whereas deep-learning approaches can recover complex structures but may remain sensitive to residual large-scale contamination. The objective of this work is therefore to close these gaps by systematically testing the FD-based deep-learning method with realistic beam effects, performing a direct performance comparison with PCA cleaning, and exploring a combined approach that leverages the advantages of both techniques. This study aims to clarify the regimes where each method is optimal and to provide a foundation for reliable HI signal recovery, which is essential for precision measurements of BAO, RSD, and HI bias with upcoming low-redshift intensity-mapping surveys.

This paper is organized as follows. Section II introduces the simulation data. In Section III, we describe a new foreground removal technique, which combines a hybrid frequency-differencing scheme with a PCA-based deep-learning approach. The performance of the method and the corresponding results are presented in Section IV. Finally, the main findings are summarized in Section V.

II. DATASET

In this study, we construct the 21-cm intensity mapping dataset using the same HI and foreground simulations as in our previous work (hereafter Paper I) [1]. We further incorporate a more advanced beam model that closely captures the characteristics of MeerKAT [18], incorporating frequency-dependent variations and beam-smoothing effects. This refinement improves the realism of our analysis and enables a more robust evaluation of the method’s performance under conditions comparable to those anticipated in forthcoming observations.

A. HI Signal and Foregrounds

For the cosmological 21-cm signal and the foreground components, we maintain the same simulation pipeline as in Paper I, employing the CRIME¹ code [59]. Below, we briefly summarize these components and refer the reader to Paper I for a detailed description.

The cosmological HI signal is simulated using a log-normal realization of the dark matter density field to model the underlying large-scale structure. The HI overdensity field is then mapped onto spherical shells corresponding to different redshifts, including the effects of redshift-space distortions (RSD) by perturbing the redshifts according to the line-of-sight peculiar velocity. The mean brightness temperature at each redshift is computed as:

$$\bar{T}_{\text{HI}}(z) = 190.55 \text{ mK} \frac{\Omega_b h (1+z)^2 x_{\text{HI}}(z)}{\sqrt{\Omega_m (1+z)^3 + \Omega_\Lambda}}, \quad (1)$$

where Ω_b , Ω_m , and Ω_Λ are the cosmological parameters; h is the dimensionless Hubble parameter; and $x_{\text{HI}}(z)$ is the neutral hydrogen fraction. The HI brightness temperature fluctuation is then given by:

$$T_{\text{HI}}(\hat{n}, z) = \bar{T}_{\text{HI}}(z) [1 + \delta_{\text{HI}}(\hat{n}, z)], \quad (2)$$

where $\delta_{\text{HI}}(\hat{n}, z)$ denotes the HI overdensity at angular position \hat{n} and redshift z .

For foregrounds, the dominant components include Galactic synchrotron radiation, Galactic and extragalactic free-free emissions, and extragalactic point sources. The Galactic synchrotron emission is modeled using the Haslam 408 MHz map [60] as a template, extrapolated to the relevant frequencies with a direction-dependent spectral index [61]. Small-scale structures, including synchrotron, free-free emissions, and point sources, are incorporated via Gaussian realizations of the angular power spectra following Santos *et al.* [30]. These components are added using parameterized models, with parameters (e.g., amplitude, spectral index, and angular power spectrum) calibrated separately for each component based on observational data. It is worth noting that the Haslam map used in the CRIME contains residual striping and point-source artifacts, which could lead to inadvertent duplication of point sources in the simulations. This concern can be alleviated by the utilization of an improved version of the Haslam map, which was reprocessed by [62]. Polarized foregrounds, including Faraday rotation effects [63], are also considered, in accordance with Paper I.

In this study, we use a map with $N_{\text{side}} = 256$ in the HEALPix pixelization scheme [64], corresponding to an angular resolution of 13.73 arcmin. We consider a frequency range spanning from 1100 to 1164 MHz, which

corresponds to a redshift range between 0.29 and 0.22. The simulated full sky is subsequently divided into 192 localized patches, each covering approximately 214.86 deg^2 sky area. For each patch, we extract a data cube with dimensions 64^3 , representing two spatial dimensions and one frequency axis. Each cube corresponds to a comoving volume approximately equivalent to a cube with a side length of $187 h^{-1} \text{ Mpc}$. The cosmological parameters are set as follows: $\Omega_m = 0.3$, $\Omega_\Lambda = 0.7$, $\Omega_b = 0.049$, $h = 0.67$, and $\sigma_8 = 0.8$.

B. Instrumental Beam Effects

To simulate the realistic observational effect, we incorporate two distinct primary beam models into our analysis: a Gaussian beam model and a more sophisticated Cosine beam model. These models are implemented to evaluate the impact of instrumental effects on the observed sky maps and to test the robustness of foreground removal methods under increasingly realistic conditions.

The Gaussian beam model serves as an idealized, simplified approximation of the primary beam response. It is modeled as a symmetric, frequency-dependent function,

$$B_G(\nu, \theta) = \exp \left[-4 \ln 2 \left(\frac{\theta}{\theta_{\text{FWHM}}(\nu)} \right)^2 \right], \quad (3)$$

where θ is the angular distance from the beam center, and $\theta_{\text{FWHM}}(\nu)$ is the full width at half maximum (FWHM) of the beam at frequency ν . The FWHM is calculated as,

$$\theta_{\text{FWHM}}(\nu) = 1.16 \frac{\lambda(\nu)}{D}, \quad (4)$$

where $\lambda(\nu) = c/\nu$ is the wavelength at frequency ν , c is the speed of light, and D is the dish diameter, which we set to $D = 13.5 \text{ m}$ to match MeerKAT specifications.

To achieve a more realistic representation of the primary beam, we adopt a Cosine beam model that captures both the main lobe and the frequency-dependent ripple structures observed in holographic measurements of the MeerKAT beam pattern [65]. The beam pattern is expressed as:

$$B_C(\nu, \theta) = \left[\frac{\cos(1.189\pi\theta/\Delta\theta_C(\nu))}{1 - 4(1.189\theta/\Delta\theta_C(\nu))^2} \right]^2, \quad (5)$$

where $\Delta\theta_C(\nu)$ represents the frequency-dependent effective beam width of the Cosine model. The effective beam width is modeled as:

$$\Delta\theta_C(\nu) = \frac{\lambda(\nu)}{D} \left[\sum_{d=0}^8 a_d \hat{\nu}^d + A \sin \left(\frac{2\pi\hat{\nu}}{T} \right) \right], \quad (6)$$

where $\hat{\nu} = \nu/\text{MHz}$ is the normalized frequency, $A = 0.1$ and $T = 20$ define the amplitude and period of the

¹ <http://intensitymapping.physics.ox.ac.uk/CRIME.html>

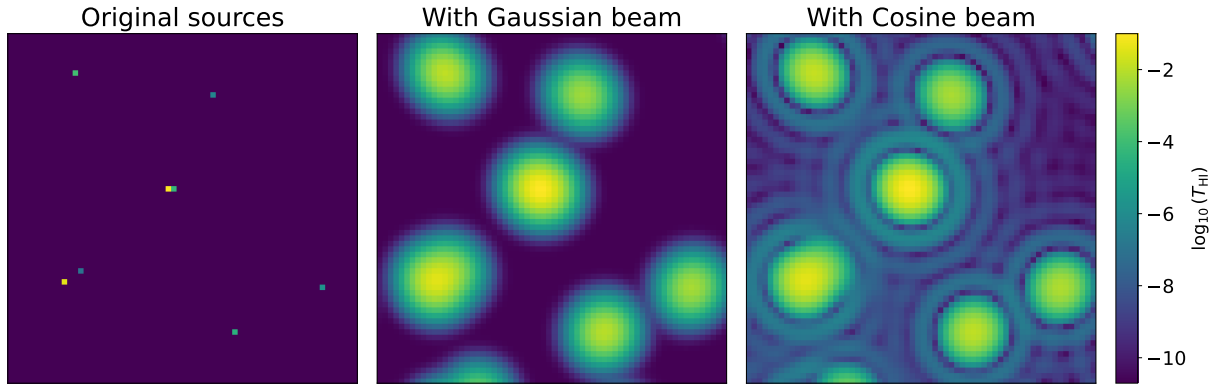


FIG. 1. Comparison of beam convolution effects on a simulated point-source map. Left: the input map containing point-like sources. Middle: the convolved map using a Gaussian beam model. Right: the convolved map using the Cosine beam model.

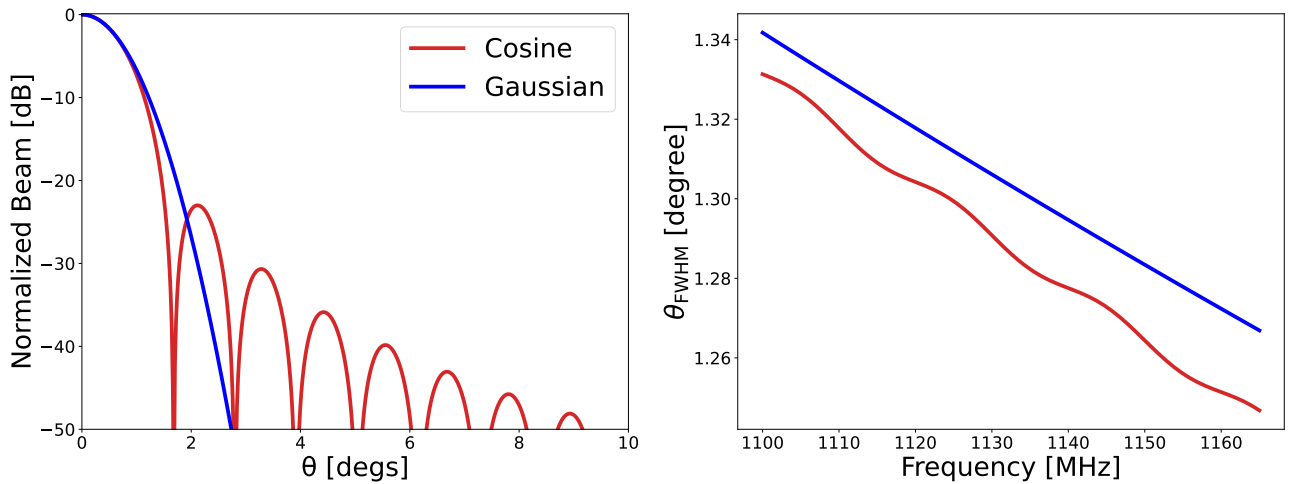


FIG. 2. (Left) Normalized angular beam profiles of the Gaussian (blue) and Cosine (red) beam models as a function of angular separation from the beam center at 1100 MHz. (Right) Frequency dependence of the FWHM for the Gaussian (blue) and Cosine (red) beam models.

sinusoidal ripple component, and the polynomial coefficients are set to: $a_d = \{3.402 \times 10^{-21}, -3.025 \times 10^{-17}, -1.17 \times 10^{-11}, -2.572 \times 10^{-10}, 3.511 \times 10^{-7}, -3.05 \times 10^{-4}, 0.1645, -50.37, 6704.28\}$, which are empirically derived from MeerKAT beam fitting data.

To illustrate the differences between the Gaussian and Cosine beam models, Figure 1 shows an example constructed from a set of randomly simulated point sources. After convolution, the Gaussian beam produces smooth and compact source profiles, whereas the Cosine beam introduces pronounced ring-like patterns and extended sidelobe structures that can mimic diffuse foreground emission. This example highlights the importance of realistic beam modeling for reliable foreground removal. The left panel of Figure 2 presents the normalized angular beam patterns at 1100 MHz. The Cosine beam exhibits pronounced sidelobes that extend to larger angular scales, whereas the Gaussian beam decreases smoothly

without significant sidelobes. These sidelobes can inject additional power on large angular scales, thereby complicating the separation of foregrounds from the cosmological 21-cm signal. The right panel shows the frequency dependence of the FWHM for both models. The Gaussian beam maintains a systematically larger FWHM due to its simple, symmetric profile that neglects detailed beam structures. In contrast, the Cosine beam captures realistic main-lobe narrowing and frequency-dependent distortions, offering a more accurate representation of instrumental chromaticity that is critical for foreground mitigation.

The inclusion of both beam models in our simulations allows for a thorough assessment of foreground mitigation techniques, ensuring that our analysis accounts for instrumental effects ranging from simplified (Gaussian) to more complex (Cosine) cases, in alignment with actual observations from the MeerKAT telescope.

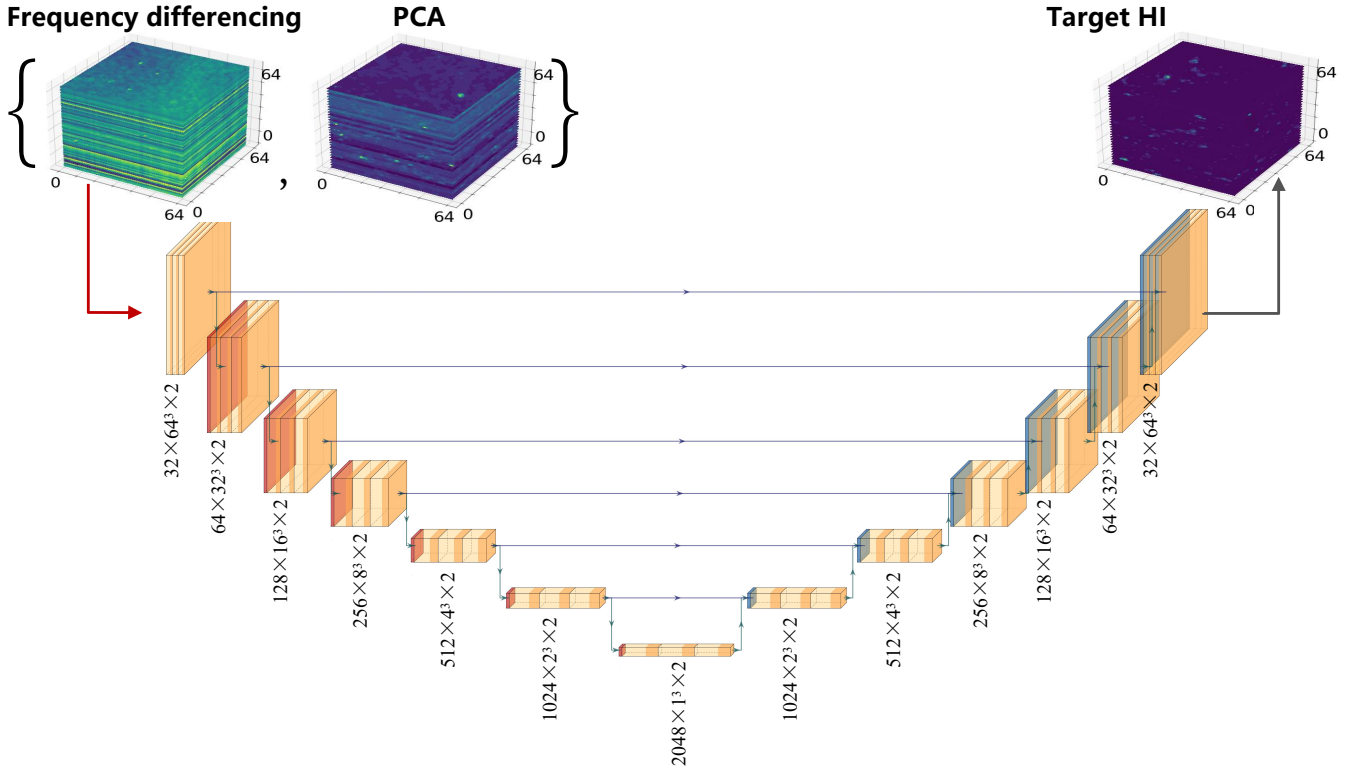


FIG. 3. Visualization of the UNet architecture. The input is a cube of size 64^3 with two channels derived from the frequency-difference and PCA-cleaned maps. The architecture consists of 13 layers, with 6 encoder layers, 6 decoder layers, and 1 bottleneck layer. Each layer includes three convolution operations with batch normalization and activation functions (except for the output layer). The annotations below each layer (e.g., $32 \times 64^2 \times 2$) denotes the number of feature maps, the spatial dimension, and the two-channel processing. Down, right, and up arrows represent max-pooling, skip connections, and transpose convolutions, respectively. This visualization was created using the `PlotNeuralNet` library.

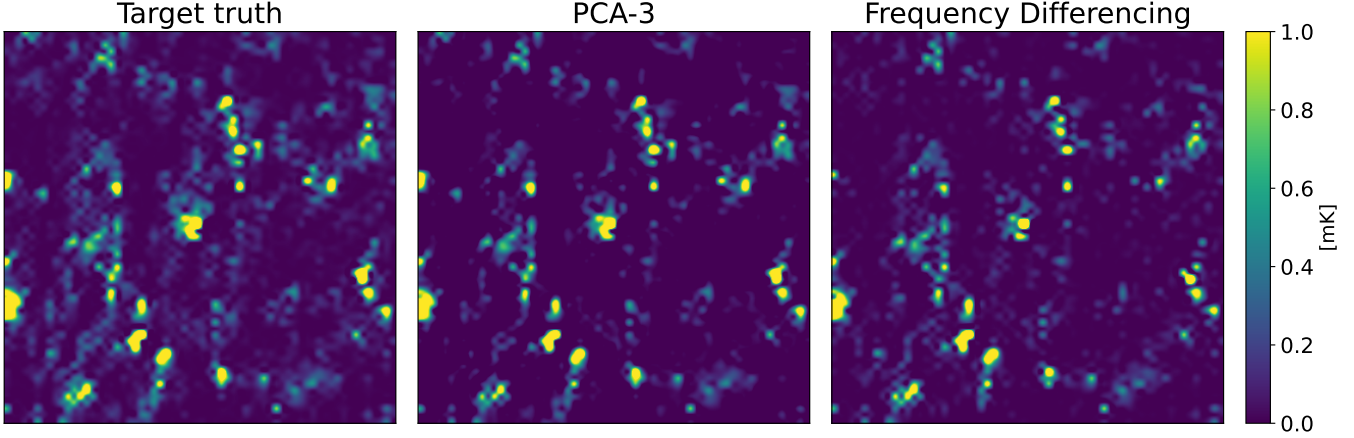


FIG. 4. Comparison of preprocessing methods applied to pure HI signal fields. From left to right, the panels show the target truth, the PCA-3 reconstruction, and the frequency differencing result, respectively.

III. FOREGROUND REMOVAL METHOD

In this section, we describe the foreground removal strategy employed in this study, which is based on deep learning techniques. Specifically, we use a UNet architecture and investigate several preprocessing methods de-

signed to improve its performance in the presence of foreground contamination and instrumental beam effects.

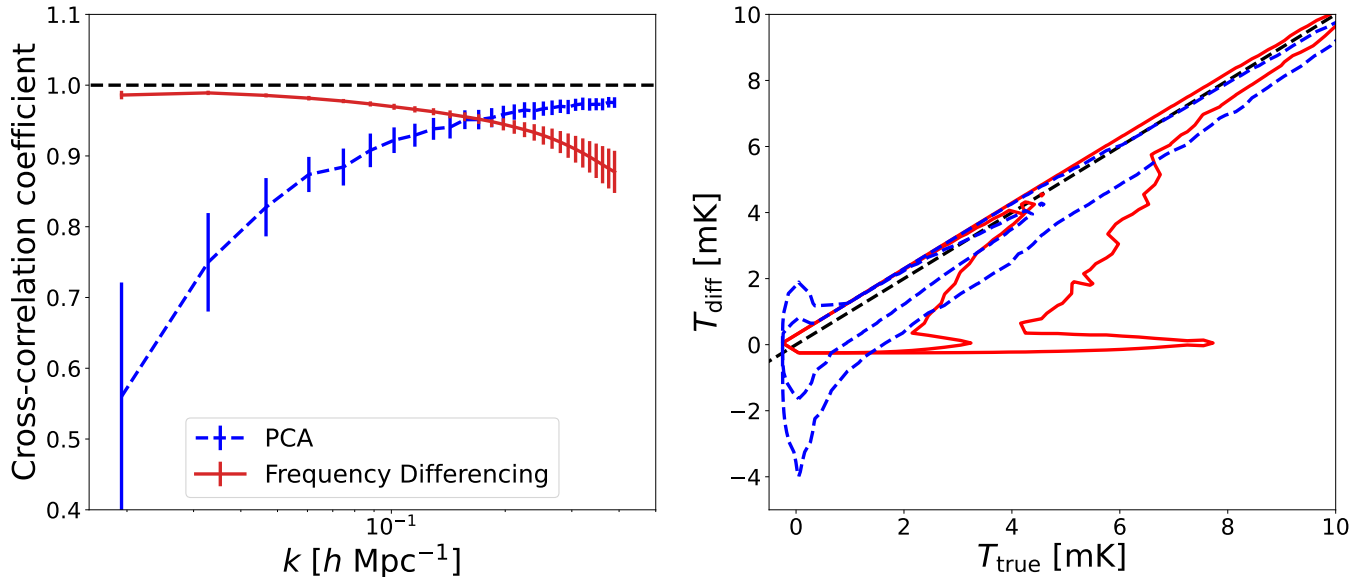


FIG. 5. Comparison of preprocessing methods applied to the pure HI fields. Left: cross-correlation coefficient $R_{\text{cross}}(k)$ between the reconstructed and true HI signals. Right: pixel-to-pixel comparison of the preprocessed temperature T_{diff} with the true temperature T_{true} , where the contours enclose 65% and 95% of the grid cells.

A. UNet Architecture

We adopt a UNet Architecture to reconstruct the cosmological 21-cm signal from foreground-contaminated and beam-convolved intensity maps. In this study, we use the same UNet structure introduced in Paper I, where a detailed description of the model configuration is provided. For completeness, we briefly summarize the key features here, with emphasis on the modifications for a two-channel input, although the design can be straightforwardly adapted to a single-channel case.

Figure 3 presents a visualization of the UNet model architecture. The network input is a cube of size 64^3 with two channels obtained from data preprocessing, which will be introduced in next subsection. The output is a single-channel HI cube of the same size. The encoder comprises six downsampling stages that progressively increase the number of feature maps from 32 to 2048, enabling the network to distinguish spectrally smooth foreground components from the rapidly varying HI signal. The decoder symmetrically upsamples these representations to recover the target field, thereby recovering the cosmological signal while suppressing residual contamination. Each block applies a pair of successive 3D convolutional layers, and the annotations in the figure (e.g., $32 \times 64^2 \times 2$) denotes the number of feature maps, the spatial dimension, and the two-channel processing. Skip connections between corresponding encoder and decoder layers preserve spatial information and enable the network to recover fine-scale HI features that might otherwise be lost during downsampling. Through this structure, the UNet implicitly learns to disentangle the spectrally smooth foregrounds from the cosmological signal

during training.

The UNet is trained in a supervised manner, with the loss function defined as the mean squared error between the network output and the ground-truth HI-only signal cube. The network processes 102 training samples each epoch, followed by 20 validation samples and 70 testing samples. Finally, we save our best model based on the minimum validation-set loss function.

B. Preprocessing Strategies

The UNet is expected to learn the separation of foregrounds from the 21-cm signal by leveraging differences in their spectral smoothness and spatial coherence. However, applying the UNet directly to raw data with full foreground complexity remains challenging, particularly under large dynamic range conditions. As demonstrated in Paper I and other studies (e.g., [51, 53]), the UNet-based method critically depends on preprocessing strategies that reduce the foreground amplitude or decorrelate its dominant spectral modes. To address this challenge, we explore three preprocessing techniques prior to UNet training, as described below.

1. Principal Component Analysis

PCA is used to exploit the spectral smoothness of foregrounds compared to the rapidly fluctuating cosmological signal. In our case, PCA is applied to each of the 192 simulated sky patches, with each 64^3 data cube reshaped into a collection of one-dimensional spectra along the fre-

quency axis. A frequency–frequency covariance matrix is computed across all spectra in each patch, serving as the basis to identify the dominant spectral modes. The resulting principal components, associated with the largest eigenvalues, are interpreted as the foreground structure and subtracted to produce a cleaned residual cube.

We subtract a fixed number of principal components (typically 3) from each frequency spectrum to produce a residual cube that suppresses most foreground power while retaining a substantial fraction of the 21-cm signal. Following `deep21`, the PCA-cleaned map is then used as input to the UNet for both training and inference. While PCA does not require any foreground modeling, it can inadvertently remove cosmological signal on large scales, necessitating careful evaluation of signal loss.

2. Frequency Differencing

Frequency differencing is a model-independent technique that exploits the spectral smoothness of foregrounds relative to the cosmological 21-cm signal. By taking differences between adjacent frequency channels along each line of sight, the spectrally coherent foreground components, which vary slowly with frequency, are effectively suppressed, while the rapidly fluctuating 21-cm signal is largely preserved.

In our implementation, the differenced cube is generated by computing the finite difference along the frequency axis:

$$\delta T(\nu_i) = T(\nu_{i+1}) - T(\nu_i), \quad (7)$$

where $T(\nu_i)$ denotes the brightness temperature at frequency ν_i . This operation results in a residual map that significantly reduces the amplitude of foregrounds without requiring any explicit modeling or eigen-decomposition.

In this study, we adopt a fixed frequency resolution of 1MHz. As demonstrated in Paper I, the choice of differencing bandwidth plays a critical role in balancing foreground suppression and signal preservation. Narrower bandwidths tend to enhance the subtraction of spectrally smooth foregrounds but can amplify noise and reduce sensitivity to the HI signal. Conversely, broader bandwidths preserve more signal but may allow residual foreground contamination to remain. Optimal performance is therefore achieved by tuning the differencing scale according to the specific characteristics of the signal and noise in the data. In our case, the 1 MHz spacing provides a reasonable trade-off given the resolution and noise properties of the simulated data.

Moreover, it is important to consider that the size of the beam (θ_{FWHM}) varies with frequency. To ensure consistency in the beam size level, we have smoothed each adjacent-band map to match their relatively lower angular resolution. This was done by convolving the higher frequency map with a Gaussian beam characterized by a

beam size of $\Delta\theta_{\text{FWHM}}$, denoted as,

$$\Delta\theta_{\text{FWHM}} = \sqrt{\theta_{\text{FWHM},\text{low}}^2 - \theta_{\text{FWHM},\text{high}}^2}. \quad (8)$$

Here $\theta_{\text{FWHM},\text{low}}$ and $\theta_{\text{FWHM},\text{high}}$ correspond to the beam size of low and high frequency, respectively. It reveals that the frequency-difference map yields a similar outcome, with a significant reduction in the range of amplitude.

In this work, we treat the differenced cube as an alternative input to the UNet and evaluate its performance relative to PCA-based preprocessing in terms of signal recovery and residual foreground suppression.

3. Hybrid Method: Dual-Channel PCA and Frequency Differencing

To leverage the complementary strengths of PCA and frequency differencing, we construct a hybrid preprocessing approach in which the outputs of both methods are used in parallel. We preprocess the input data cube independently using PCA and frequency differencing, yielding two separate residual maps. These are then combined to form a two-channel input for the UNet.

To motivate the hybrid preprocessing approach, we compare the performance of PCA and frequency differencing by applying each method to pure HI signal maps that don't include any foreground. As shown in Figure 4, the PCA reconstruction (middle panel) preserves most of the bright small-scale structures but also suppresses part of the diffuse background, leading to a noticeable loss of large-scale information. In contrast, the frequency differencing method (right panel) better retains the diffuse large-scale features but introduces residual striping and artificial patterns, which distort small-scale structures. This complementary behavior highlights the potential of a hybrid preprocessing strategy, which aims to combine the strengths of both methods while mitigating their respective limitations.

Furthermore, Figure 5 shows the cross-correlation coefficient between the recovered and true HI fields (left panel) and the pixel-to-pixel temperature comparison (right panel). The cross-correlation results show that frequency differencing (red) achieves nearly perfect correlation on large scales ($k \lesssim 0.1 h \text{ Mpc}^{-1}$), while PCA (blue) significantly underestimates the signal due to the removal of large-scale modes. However, at smaller scales, PCA recovers the correlation more accurately, whereas frequency differencing gradually loses performance as residual distortions dominate. The pixel-to-pixel confirms that the PCA reconstruction (blue) scatters more broadly around the one-to-one line, especially at low temperatures, which indicates a loss of diffuse components. By contrast, frequency differencing (red) follows the one-to-one relation more closely for diffuse emission but introduces systematic deviations and distortions for bright pixels. These results highlight the complementary nature of the two

methods, with PCA being more reliable at preserving small-scale structures and frequency differencing more effective at retaining large-scale diffuse features.

These complementary behaviors highlight the benefit of the hybrid strategy, in which both PCA-cleaned and frequency-differenced maps are used as two-channel inputs to the UNet. This configuration enables the network to simultaneously exploit the large-scale accuracy of frequency differencing and the improved small-scale fidelity of PCA-based suppression. We assess the effectiveness of this dual-channel hybrid method by comparing its performance against the single-channel PCA-only and frequency-differencing-only configurations in terms of signal recovery and residual foreground contamination.

IV. RESULTS

In this section, we evaluate the performance of the UNet-based foreground removal method under varying observational conditions. Specifically, we consider three progressively scenarios: (i) input maps containing only the 21-cm signal and foregrounds; (ii) maps further convolved with a Gaussian instrumental beam; and (iii) maps convolved with a more realistic, frequency-dependent Cosine beam profile. For each scenario, we compare the effectiveness of three preprocessing strategies, namely PCA, frequency differencing (FD), and their combination (Hybrid), in enhancing the recovery of the underlying HI signal. Results from the PCA-only method are included as a baseline reference. For all PCA-related approaches, three principal components are removed to suppress the dominant smooth spectral modes.

A. HI + Foreground: Ideal Instrument Case

We begin our analysis with the first scenario. Figure 6 presents 2D slices of the target HI field alongside the reconstructed fields obtained using the FD+UNet, PCA+UNet, and PCA-only methods, as labeled above each panel. Both UNet-based approaches yield reconstructions that are visually consistent with the ground truth, while the PCA-only result shows a noticeable suppression of temperature distribution due to the aggressive removal of spectral modes.

Figure 7 presents a quantitative comparison across several statistical diagnostics. From left to right, the panels show the temperature distributions, the pixel-to-pixel correlation between reconstructed and true fields, and the correlation coefficient as a function of frequency. Both FD+UNet and PCA+UNet reproduce the HI histogram with high fidelity over the entire dynamic range, whereas the PCA-only reconstruction is systematically biased toward lower amplitudes. The pixel-level comparison further indicates that the two UNet-based models preserve an almost perfectly linear relation relative to the target

temperatures, while the PCA-only case shows a biased correlation with systematically reduced amplitudes. The correlation coefficients remain above 0.99 across the full band for both UNet-based approaches, confirming their stable and accurate recovery of the HI signal, in contrast to the substantially degraded correlations produced by PCA-only. A minor decline at the band edges appears in the FD+UNet case, which arises from boundary effects introduced by the finite-differencing operation. Because the first and last channels lack symmetric neighboring information, the differencing step cannot be applied consistently at those locations, resulting in reduced accuracy near the frequency boundaries.

Figure 8 compares the ratios of the auto-power spectrum (left) and cross-power spectrum (right) between the recovered and true fields. For the recovered $P(k)$, the error bars represent the 1σ variance estimated from the test samples. The black error bars on the reference line are derived from the theoretical variance associated with the finite number of Fourier modes in a limited volume [66], given by

$$\Delta P(k) = \frac{P(k)}{\sqrt{N_k}}, \quad (9)$$

where N_k is the number of independent k -modes in each bin. Both FD+UNet and PCA+UNet accurately recover the power spectra across the full k -range. By contrast, PCA alone performs poorly at all scales, especially at low k , where it suffers significant signal loss.

Finally, Figure 9 shows the 2D power spectrum ratios in the $(k_{\perp}, k_{\parallel})$ plane for the auto (left) and cross (right) spectra. Both FD+UNet and PCA+UNet yield power spectra that closely trace the shape and amplitude of the target HI field, while PCA-only again shows significant power suppression, especially near the low- k_{\parallel} modes where smooth foregrounds dominate.

In this idealized case without instrumental convolution, both FD+UNet and PCA+UNet deliver high-fidelity reconstructions of the 21-cm signal, significantly outperforming the PCA-only baseline. The UNet is capable of recovering signal components that are partially lost during the preprocessing step by learning spatial and spectral patterns from the training data. These results validate the effectiveness of applying deep learning-based methods, even under simple conditions, and establish a foundation for more complex scenarios involving instrumental systematics.

B. HI + Foreground with Gaussian Beam Convolution

We now evaluate the performance of the methods in the presence of instrumental smoothing by convolving the HI+foreground maps with a symmetric Gaussian beam. Figure 10 shows 2D slices of the target truth and the reconstructed HI fields from FD+UNet, PCA+UNet, Hybrid+UNet, and PCA-only. All UNet-based methods re-

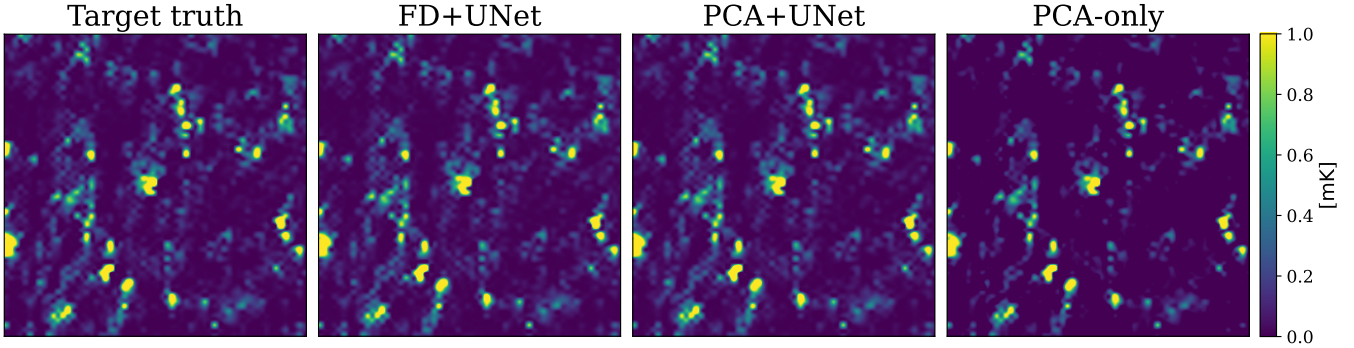


FIG. 6. Comparison of reconstructed HI maps without beam effects. From left to right, the panels show the true HI signal (Target truth), the FD+UNet reconstruction, the PCA+UNet reconstruction, and the PCA-only reconstruction.

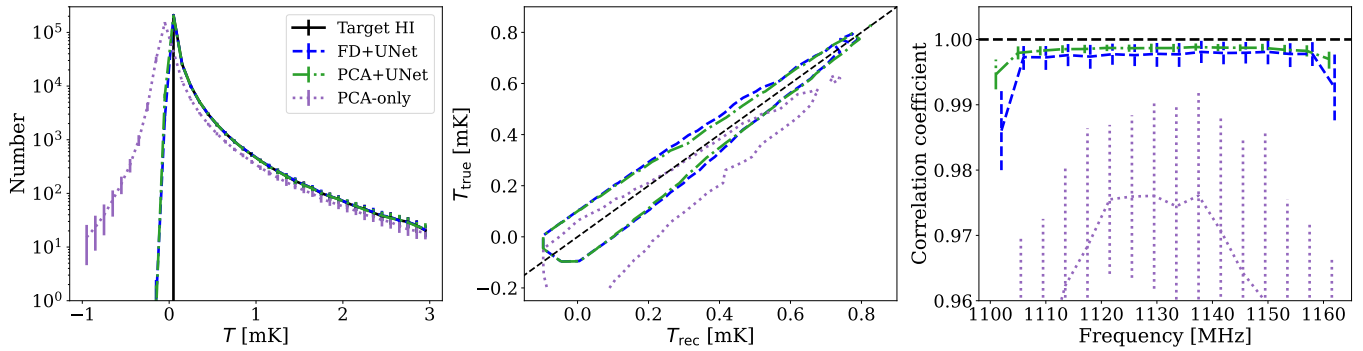


FIG. 7. Diagnostics of reconstruction performance without beam effects. Left: temperature distribution of the reconstructed and true HI fields. Middle: pixel-to-pixel correlation between reconstructed and true fields, with contours enclosing about 95% of the grid cells. Right: Correlation coefficients as a function of frequency. The blue dashed, green dash-dotted, and purple dotted lines correspond to the FD+UNet, PCA+UNet, and PCA-only cases. Error bars indicate the 1σ scatter across samples.

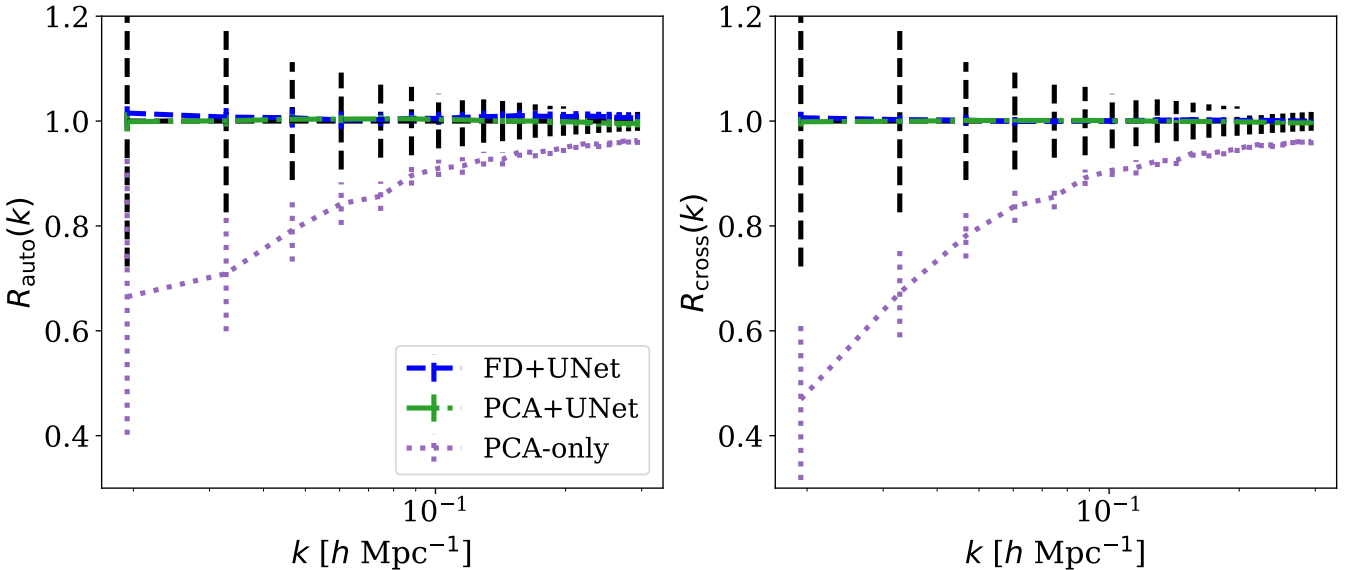


FIG. 8. Auto- (left) and cross-power (right) spectrum ratios without beam convolution. The results of FD+UNet (blue dashed), PCA+UNet (green dash-dotted), and PCA-only reconstruction (purple dotted) are shown for comparison. The black dashed error bars represent the theoretical uncertainties computed using Equation (9).

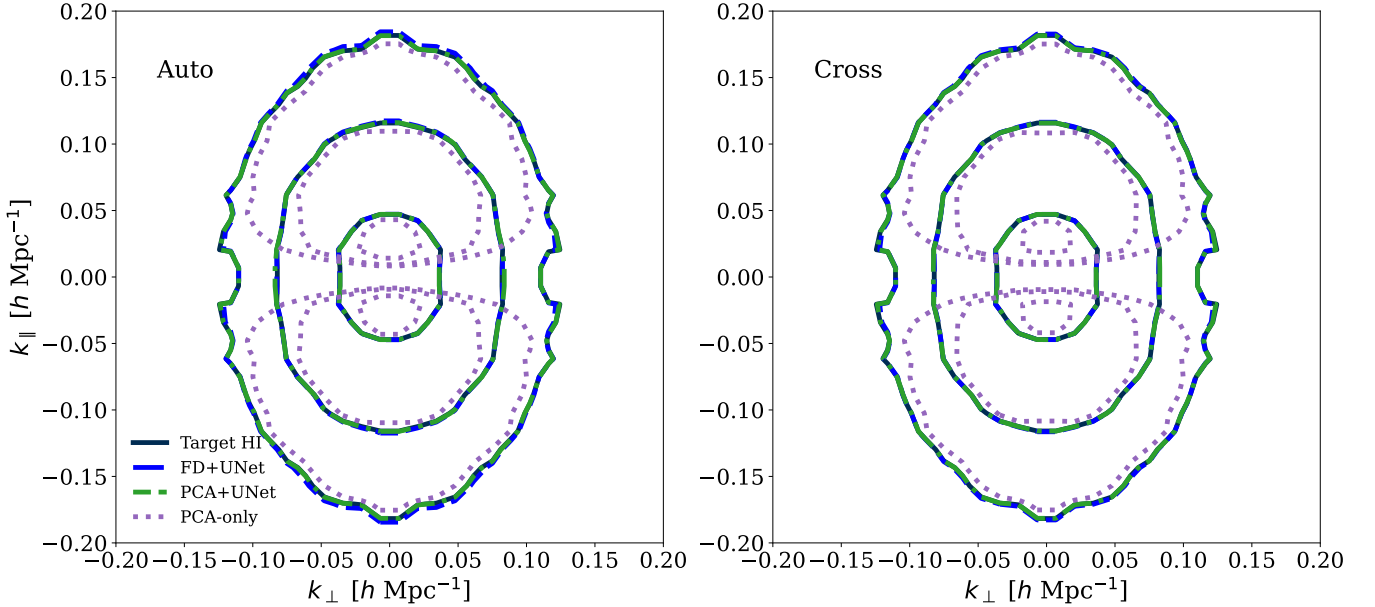


FIG. 9. Comparison of two-dimensional power spectra $P(k_{\perp}, k_{\parallel})$ without beam effects. Left: auto-power spectra of the reconstructed HI fields. Right: cross-power spectra between the reconstructed and true HI fields. Contours correspond to the target HI field (black solid), FD+UNet (red dashed), PCA+UNet (blue dash-dotted), and PCA-only (green dotted).

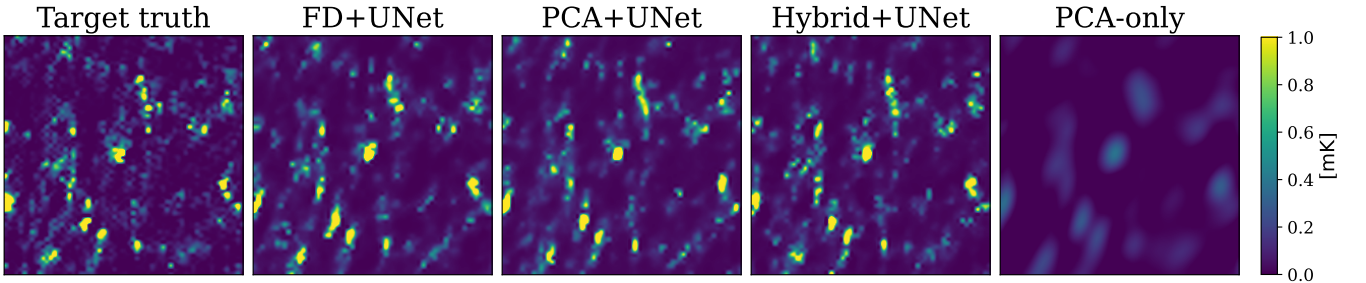


FIG. 10. Same as Figure 6, but with Gaussian beam convolution applied. The results from the hybrid method are also included for comparison.

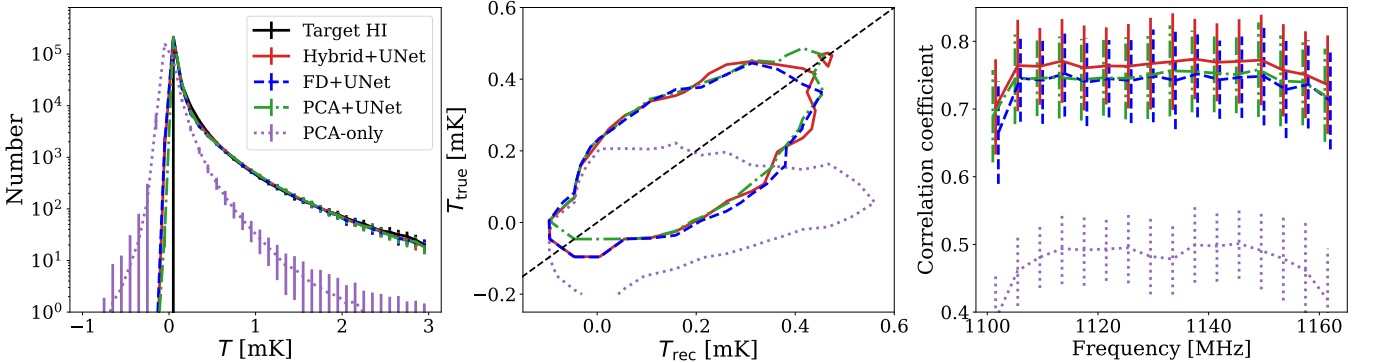


FIG. 11. Same as Figure 7, but with Gaussian beam convolution applied. The results from the hybrid method are also included for comparison.

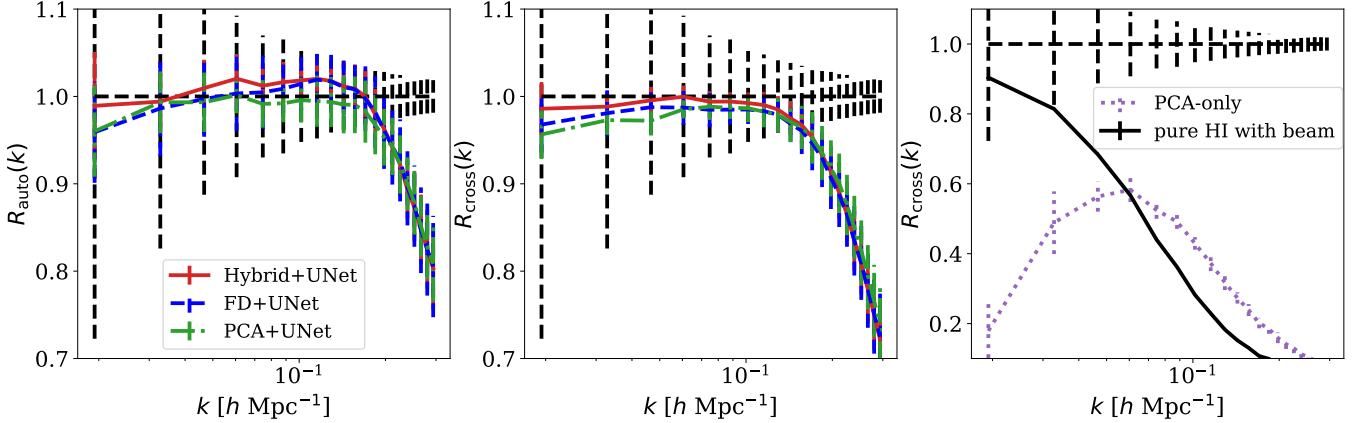


FIG. 12. Auto- and cross-power spectrum ratios under Cosine beam convolution. The first two panels show the results of the Hybrid+UNet (red solid), FD+UNet (blue dashed), and PCA+UNet (green dash-dotted) models, while the third panel presents the pure HI field convolved with the Cosine beam (black solid) and the PCA-only reconstruction (purple dotted) for reference. The colored error bars indicating the 1σ variance across the samples, and the black dashed error bars are computed using Equation (9).

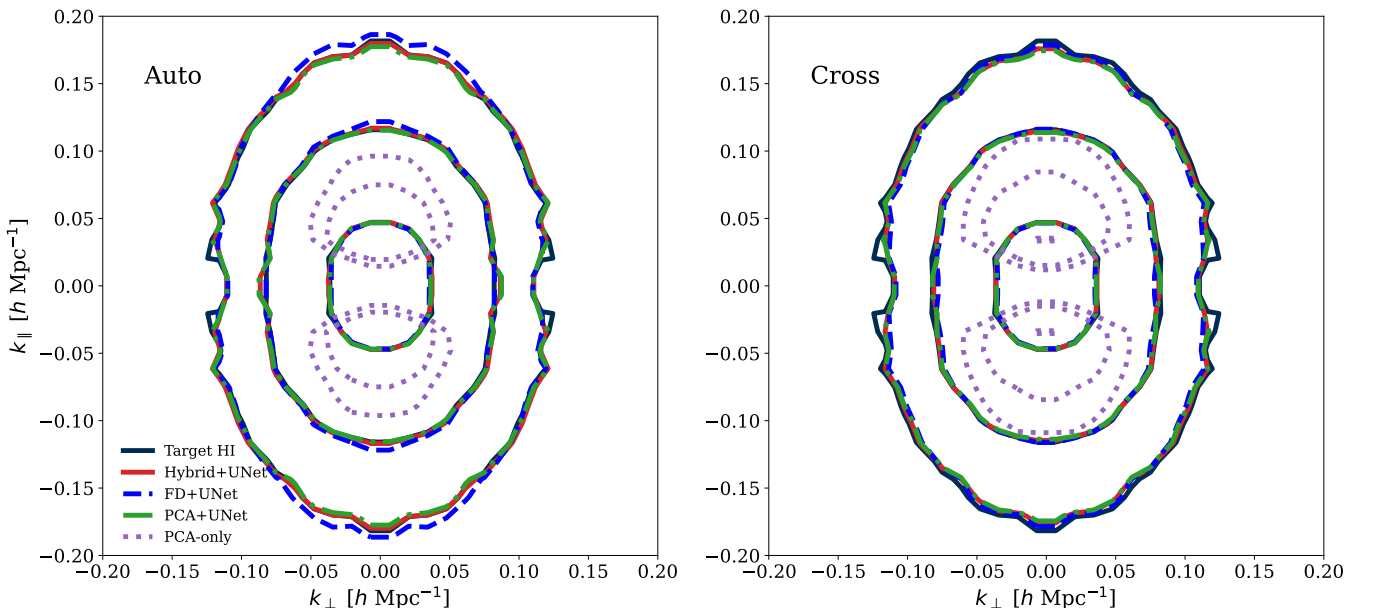


FIG. 13. Same as Figure 9, but with Gaussian beam convolution applied. The results from the hybrid method are also included for comparison.

tain the large-scale morphology of the underlying HI distribution, while the PCA-only result suffers from severe suppression and loss of small-scale structures. Notably, the hybrid method produces the most visually accurate reconstruction, recovering both the peak amplitudes and the diffuse structures with high fidelity.

Figure 11 presents the temperature distributions (left panel), pixel-to-pixel correlation (middle panel), and correlation coefficient (left panel). All UNet-based methods reproduce the overall shape of the temperature distribution, with only minor differences visible among them. In the pixel-to-pixel correlation, FD+UNet shows a slightly

larger spread at low temperatures, suggesting better retention of faint diffuse components, while PCA+UNet more closely follows the diagonal at higher temperatures, indicating improved recovery of strong peaks. This trend is consistent with Figure 5. Frequency differencing preserves large-scale diffuse emission but introduces distortions at high amplitudes, whereas PCA suppresses some large-scale modes yet retains compact bright structures more accurately. The hybrid method combines these strengths and achieves the tightest overall correlation with the ground truth. The correlation-coefficient curves show that all UNet-based models achieve high correla-

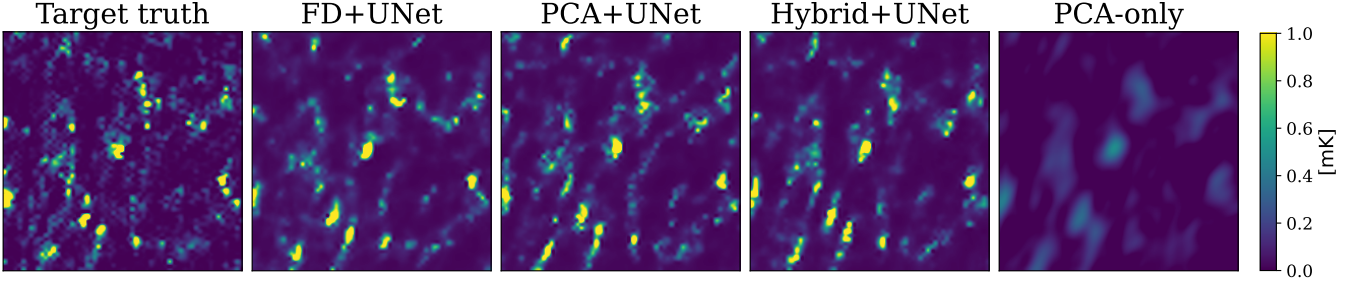


FIG. 14. Same as Figure 6, but with Cosine beam convolution applied. The results from the hybrid method are also included for comparison.

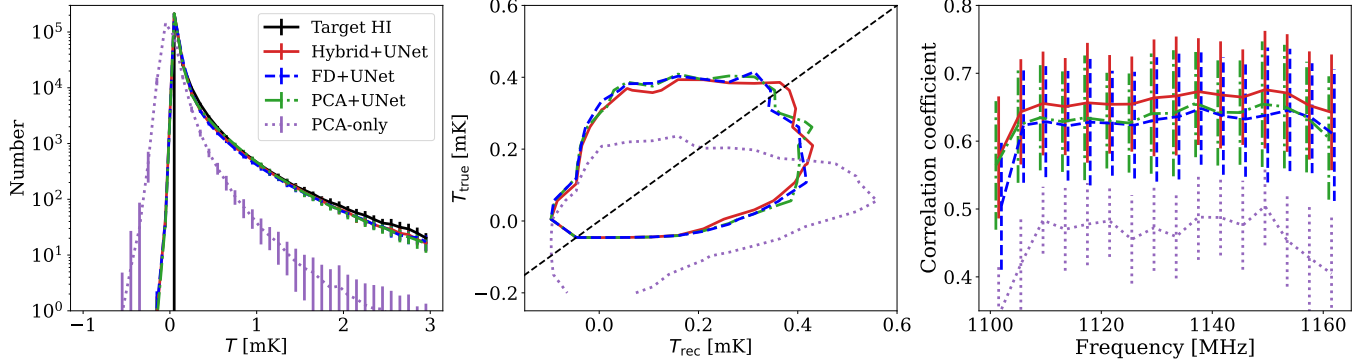


FIG. 15. Same as Figure 7, but with Cosine beam convolution applied. The results from the hybrid method are also included for comparison.

tions across the band, with the hybrid method consistently reaching the largest values, while FD+UNet and PCA+UNet remain slightly lower but still closely follow the ground truth. In contrast, the PCA-only reconstruction shows substantially reduced amplitudes and lower correlations, highlighting its limited ability to recover the HI signal in the presence of Gaussian beam smoothing.

Figure 12 presents the auto- and cross-power spectrum ratios under Gaussian beam convolution. At large scales ($k < 0.1 h \text{ Mpc}^{-1}$), all UNet-based methods recover power ratios close to unity, indicating that the large-scale structures are well reconstructed. Among them, the hybrid model achieves the best cross-correlation consistency by combining the large-scale mode preservation of frequency differencing with the effective foreground suppression of PCA, thereby reducing scale-dependent deviations. At smaller scales ($k > 0.1 h \text{ Mpc}^{-1}$), all methods show a pronounced decline in both the auto- and cross-power ratios relative to Figure 8, primarily reflecting the loss of small-scale power caused by the beam smoothing of fine structures.

The third panel of Figure 12 provides additional context by including the pure HI field convolved with a Gaussian beam and the PCA-only reconstruction as reference cases. The beam-convolved HI serves as the expected baseline illustrating the inherent loss of small-scale power due to instrumental effects, while the PCA result repre-

sents the performance of a conventional linear method. Compared to these references, all UNet-based models achieve significantly higher cross-correlation across scales, demonstrating their ability to partially compensate for the beam-induced suppression and recover finer structural information beyond what PCA alone can achieve.

Overall, these results demonstrate that Gaussian beam smoothing suppresses fine-scale features, but UNet-based reconstructions substantially alleviate this effect. All three methods clearly outperform PCA-only, and the hybrid method delivers the most consistent results, particularly at large scales. This highlights the advantage of combining complementary preprocessing strategies when restoring the 21-cm signal under instrumental smoothing.

C. HI + Foreground with Cosine Beam Convolution

We next assess the reconstruction performance under the more realistic Cosine beam model, which introduces frequency-dependent main-lobe narrowing and sidelobe structures that more closely mimic actual instrumental effects. Figure 14 shows 2D slices of the target HI field and the reconstructed maps under Cosine beam convo-

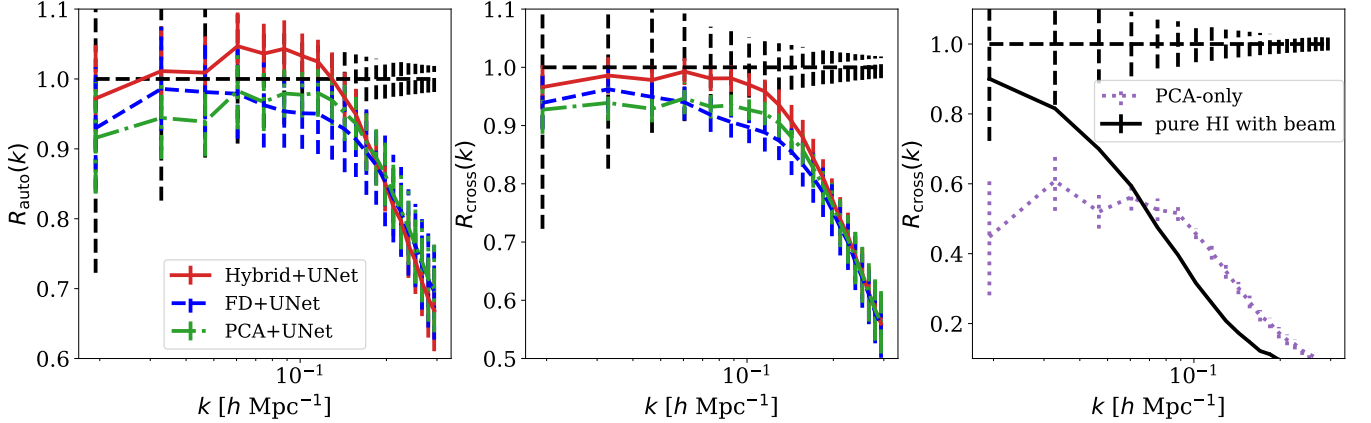


FIG. 16. Same as Figure 12, but with Cosine beam convolution applied.

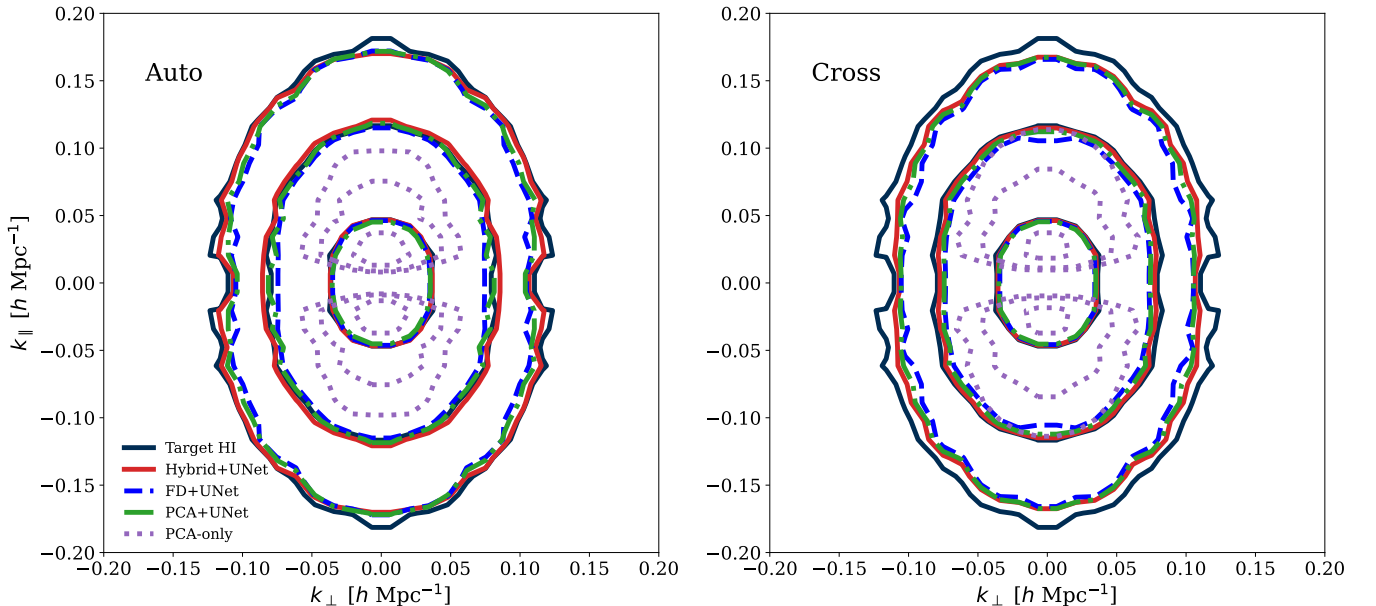


FIG. 17. Same as Figure 9, but with Cosine beam convolution applied. The results from the hybrid method are also included for comparison.

lution. Similar to the Gaussian beam case, all three UNet-based methods successfully recover the large-scale morphology of the HI distribution, whereas the PCA-only result remains strongly suppressed and misses much of the small-scale structure. Among the UNet reconstructions, the hybrid method most closely matches the target map, capturing both bright peaks and diffuse regions with higher fidelity. FD+UNet and PCA+UNet also yield visually consistent reconstructions, though with slightly greater structural differences relative to the target.

Figure 15 presents the temperature distributions (left panel), pixel-to-pixel correlations (middle panel), and correlation coefficient (right panel) under Cosine beam convolution. Compared with the no-beam (Figure 7) and Gaussian beam (Figure 11) cases, all methods show in-

creased scatter and stronger departures from the true statistics, reflecting the stronger frequency dependence and sidelobe complexity of the Cosine beam. Nevertheless, all three UNet-based methods continue to recover the overall brightness distribution and maintain correlations with the target field, whereas PCA-only remains severely biased and strongly suppressed. Among the UNet approaches, the hybrid method achieves the highest correlation coefficients across the band, indicating a modest but persistent advantage under these more challenging beam conditions.

Figure 16 shows the auto- and cross-power spectrum ratios under Cosine beam convolution. Compared with the no-beam and Gaussian beam cases, all three UNet-based methods experience stronger suppression, which is already visible at large scales ($k < h \text{ Mpc}^{-1}$)

and increases toward higher k . At $k < 0.1 h \text{ Mpc}^{-1}$, both FD+UNet and PCA+UNet underestimate the cross-power by approximately 5-8%, with the deficit exceeding 20% around $k \simeq 0.2 h \text{ Mpc}^{-1}$. In contrast, the hybrid model remains statistically consistent with unity within the 1σ level across large scales and exhibits relatively smaller deviations at smaller scales, indicating a more accurate recovery of the true power spectrum. This again demonstrates that the hybrid approach most effectively alleviates the large-scale suppression caused by the frequency-dependent sidelobes of the Cosine beam. The third panel includes the pure HI field convolved with the Cosine beam and the PCA-only reconstruction for reference. The strong suppression in the beam-convolved HI case illustrates the intrinsic loss of small-scale power, while the UNet-based models recover much of this loss and achieve noticeably better correlations than the PCA result.

Figure 17 presents the 2D auto- and cross-power spectra $P(k_{\perp}, k_{\parallel})$ under Cosine beam convolution. All three UNet-based methods reproduce the overall anisotropic structure of the target power spectra, with contours that broadly follow the true distribution across the $k_{\perp}-k_{\parallel}$ plane. Compared with the Gaussian beam case, the Cosine beam leads to an overall reduction in power across the $k_{\perp}-k_{\parallel}$ plane but does not significantly distort the anisotropic pattern. The hybrid maintains the closest match to the target, though the differences from FD+UNet and PCA+UNet remain relatively small, indicating that all three approaches achieve comparable recovery of the 2D power spectra under this more challenging beam model.

Therefore, the UNet-based methods remain effective in recovering the main features of the HI field under the Cosine beam. Notably, the hybrid method shows a clear advantage, achieving much closer agreement with the true power spectra, particularly at large scales. These results highlight the value of combining complementary preprocessing strategies to mitigate the impact of realistic beam effects.

V. SUMMARY AND CONCLUSION

In this work we developed a deep learning framework for mitigating foreground contamination and instrumental beam effects in 21-cm intensity mapping. The method is built on a UNet architecture and is tested using three alternative preprocessing strategies: FD, PCA, and a two channel hybrid combination of the two. We tested the approaches using simulated maps with realistic foregrounds and evaluated its performance under Gaussian beam convolution and a frequency dependent Cosine beam model, which represent increasingly demanding observational conditions.

The reconstructed maps show clear differences between the deep learning approaches and the PCA only baseline once foregrounds and beam convolution are in-

cluded. PCA only removes smooth spectral components and therefore suppresses a significant fraction of the true signal after the combined action of the foregrounds and the beam modifies the spectral structure of the sky. This results in reduced amplitudes and noticeably lower correlation with the truth. In comparison, the UNet-based reconstructions retain substantially more of the underlying fluctuations, indicating that the network learns to alleviate the residual foreground contamination and also corrects the distortions produced by both the Gaussian beam and the more complex Cosine beam.

Our analysis of the UNet based reconstructions also shows that the preprocessing strategies contribute complementary strengths. Frequency differencing preserves large scale diffuse emission but introduces artificial structures in regions of high brightness temperature, while PCA recovers most of the bright small scale features but suppresses part of the large scale modes. These observations motivate the (FD,PCA)+UNet framework, which combines both inputs through a two channel architecture to capture the advantages of each preprocessing technique.

The hybrid preprocessing approach delivers the strongest performance, particularly in the presence of the Cosine beam. In this case, the cross-correlation power spectrum remains statistically consistent with unity at the 1σ level across the large scale range ($k < 0.1, h, \text{Mpc}^{-1}$) and exhibits relatively smaller deviations at higher k . In contrast, the FD+UNet and PCA+UNet methods both show clear suppression, underestimating the cross power spectra by roughly 5-8% at $k < 0.1, h, \text{Mpc}^{-1}$ and by more than 20% at $k \simeq 0.2, h, \text{Mpc}^{-1}$.

Overall, our findings show that deep learning, particularly when coupled with hybrid preprocessing, provides a powerful and resilient strategy for mitigating both foregrounds and beam effects in 21-cm intensity mapping. The ability to recover unbiased large-scale structure even under frequency-dependent beam distortions is essential for precision cosmological applications such as BAO and RSD measurements in upcoming surveys including MeerKAT and SKA. Future work will incorporate thermal noise, calibration systematics, and real observational data, moving toward a fully end-to-end analysis pipeline for next-generation 21-cm cosmology.

ACKNOWLEDGMENTS

This work is supported by the National SKA Program of China (2022SKA0110200 and 2022SKA0110202) and the National Natural Science Foundation of China (Nos.12103037, 12473097, 12203038). F.S acknowledges the support from the State Key Laboratory of Dark Matter Physics and the Young Data Scientist Program of the China National Astronomical Data Center (No.NADC2025YDS-01). This work is supported by the China Manned Space Project with Nos. CMS-

CSST-2021 (A02, A03, B01), and Guangdong Basic and Applied Basic Research Foundation (2024A1515012309). This work is supported by Natural Science Basic Research Program of Shaanxi (Program No. 2025JC-

YBMS-016). The authors acknowledge the Beijing Super Cloud Center (BSCC) for providing HPC resources that have contributed to the research results reported in this paper.

[1] F. Shi, H. Chang, L. Zhang, H. Shan, J. Zhang, S. Zhou, M. Jiang, and Z. Wang, 21-cm foreground removal using AI and the frequency-difference technique, *Phys. Rev. D* **109**, 063509 (2024), arXiv:2310.06518 [astro-ph.CO].

[2] S. Bharadwaj, B. B. Nath, and S. K. Sethi, Using HI to probe large scale structures at $z \sim 3$, *Journal of Astrophysics and Astronomy* **22**, 21 (2001), arXiv:astro-ph/0003200 [astro-ph].

[3] R. A. Battye, R. D. Davies, and J. Weller, Neutral hydrogen surveys for high-redshift galaxy clusters and protoclusters, *MNRAS* **355**, 1339 (2004), arXiv:astro-ph/0401340 [astro-ph].

[4] J. B. Peterson, R. Aleksan, R. Ansari, K. Bandura, D. Bond, J. Bunton, K. Carlson, T.-C. Chang, F. DeJongh, M. Dobbs, S. Dodelson, H. Darhmaoui, N. Gnedin, M. Halpern, C. Hogan, J.-M. Le Goff, T. T. Liu, A. Legouri, A. Loeb, K. Loudiyi, C. Magneville, J. Marriner, D. P. McGinnis, B. McWilliams, M. Moniez, N. Palanque-Delabruille, R. J. Pasquinelli, U.-L. Pen, J. Rich, V. Scarpine, H.-J. Seo, K. Sigurdson, U. Seljak, A. Stebbins, J. H. Steffen, C. Stoughton, P. T. Timbie, A. Vallinotto, and C. Teche, 21-cm Intensity Mapping, in *astro2010: The Astronomy and Astrophysics Decadal Survey*, Vol. 2010 (2009) p. 234, arXiv:0902.3091 [astro-ph.IM].

[5] J. S. B. Wyithe and A. Loeb, The 21-cm power spectrum after reionization, *MNRAS* **397**, 1926 (2009), arXiv:0808.2323 [astro-ph].

[6] T.-C. Chang, U.-L. Pen, J. B. Peterson, and P. McDonald, Baryon Acoustic Oscillation Intensity Mapping of Dark Energy, *Phys. Rev. Lett.* **100**, 091303 (2008), arXiv:0709.3672 [astro-ph].

[7] H.-J. Seo, S. Dodelson, J. Marriner, D. McGinnis, A. Stebbins, C. Stoughton, and A. Vallinotto, A Ground-based 21 cm Baryon Acoustic Oscillation Survey, *Astrophys. J.* **721**, 164 (2010), arXiv:0910.5007 [astro-ph.CO].

[8] A. Liu and J. R. Shaw, Data Analysis for Precision 21 cm Cosmology, *PASP* **132**, 062001 (2020), arXiv:1907.08211 [astro-ph.IM].

[9] P.-J. Wu, Y. Li, J.-F. Zhang, and X. Zhang, Prospects for measuring dark energy with 21 cm intensity mapping experiments: A joint survey strategy, *Science China Physics, Mechanics, and Astronomy* **66**, 270413 (2023), arXiv:2212.07681 [astro-ph.CO].

[10] M. Amiri, K. Bandura, T. Chen, M. Deng, M. Dobbs, M. Fandino, S. Foreman, M. Halpern, A. S. Hill, G. Hinshaw, C. Höfer, J. Kania, T. L. Landecker, J. MacEachern, K. Masui, J. Mena-Parra, N. Milutinovic, A. Mirhosseini, L. Newburgh, R. Nitsche, A. Ordog, U.-L. Pen, T. Pinsonneault-Marotte, A. Polzin, A. Reda, A. Renard, J. R. Shaw, S. R. Siegel, S. Singh, R. Smegal, I. Tretyakov, K. van Gassen, K. Vanderlinde, H. Wang, D. V. Wiebe, J. S. Willis, and D. Wulf, An Overview of CHIME, the Canadian Hydrogen Intensity Mapping Experiment, *ApJS* **261**, 29 (2022), arXiv:2201.07869 [astro-ph.IM].

[11] CHIME Collaboration, M. Amiri, K. Bandura, A. Boskovic, T. Chen, J.-F. Cliche, M. Deng, N. Denman, M. Dobbs, M. Fandino, S. Foreman, M. Halpern, D. Hanna, A. S. Hill, G. Hinshaw, C. Höfer, J. Kania, P. Klages, T. L. Landecker, J. MacEachern, K. Masui, J. Mena-Parra, N. Milutinovic, A. Mirhosseini, L. Newburgh, R. Nitsche, A. Ordog, U.-L. Pen, T. Pinsonneault-Marotte, A. Polzin, A. Reda, A. Renard, J. R. Shaw, S. R. Siegel, S. Singh, R. Smegal, I. Tretyakov, K. van Gassen, K. Vanderlinde, H. Wang, D. V. Wiebe, J. S. Willis, and D. Wulf, An Overview of CHIME, the Canadian Hydrogen Intensity Mapping Experiment, *ApJS* **261**, 29 (2022), arXiv:2201.07869 [astro-ph.IM].

[12] X. Chen, Radio detection of dark energy—the Tianlai project, *Scientia Sinica Physica, Mechanica & Astronomica* **41**, 1358 (2011).

[13] Y. Xu, X. Wang, and X. Chen, Forecasts on the Dark Energy and Primordial Non-Gaussianity Observations with the Tianlai Cylinder Array, *Astrophys. J.* **798**, 40 (2015), arXiv:1410.7794 [astro-ph.CO].

[14] F. Wu, J. Li, S. Zuo, X. Chen, S. Das, J. P. Marriner, T. M. Oxholm, A. Phan, A. Stebbins, P. T. Timbie, R. Ansari, J.-E. Campagne, Z. Chen, Y. Cong, Q. Huang, J. Kwak, Y. Li, T. Liu, Y. Liu, C. Niu, C. Osinga, O. Perdereau, J. B. Peterson, J. Podczerwinski, H. Shi, G. Siebert, S. Sun, H. Tian, G. S. Tucker, Q. Wang, R. Wang, Y. Wang, Y. Wu, Y. Xu, K. Yu, Z. Yu, J. Zhang, J. Zhang, and J. Zhu, The Tianlai dish pathfinder array: design, operation, and performance of a prototype transit radio interferometer, *MNRAS* **506**, 3455 (2021), arXiv:2011.05946 [astro-ph.IM].

[15] O. Perdereau, R. Ansari, A. Stebbins, P. T. Timbie, X. Chen, F. Wu, J. Li, J. P. Marriner, G. S. Tucker, Y. Cong, S. Das, Y. Li, Y. Liu, C. Magneville, J. B. Peterson, A. Phan, L. Robinthal, S. Sun, Y. Wang, Y. Wu, Y. Xu, K. Yu, Z. Yu, J. Zhang, J. Zhang, and S. Zuo, The Tianlai dish array low- z surveys forecasts, *MNRAS* **517**, 4637 (2022), arXiv:2205.06086 [astro-ph.CO].

[16] R. A. Battye, I. W. A. Browne, C. Dickinson, G. Heron, B. Maffei, and A. Pourtsidou, H I intensity mapping: a single dish approach, *MNRAS* **434**, 1239 (2013), arXiv:1209.0343 [astro-ph.CO].

[17] E. Abdalla, E. G. M. Ferreira, R. G. Landim, A. A. Costa, K. S. F. Fornazier, F. B. Abdalla, L. Barosi, F. A. Brito, A. R. Queiroz, T. Villela, B. Wang, C. A. Wünsche, A. Marins, C. P. Novaes, V. Liccardo, C. Shan, J. Zhang, Z. Zhang, Z. Zhu, I. Browne, J. Delabrouille, L. Santos, M. V. dos Santos, H. Xu, S. Anton, R. Battye, T. Chen, C. Dickinson, Y.-Z. Ma, B. Maffei, E. J. de Mericia, P. Motta, C. H. N. Otobone, M. W. Peel, S. Roychowdhury, M. Remazeilles, R. M. Ribeiro, Y. Sang, J. R. L. Santos, J. F. R. dos Santos, G. B. Silva, F. Vieira, J. Vieira, L. Xiao, X. Zhang, and Y. Zhu, The

BINGO project. I. Baryon acoustic oscillations from integrated neutral gas observations, *A&A* **664**, A14 (2022), arXiv:2107.01633 [astro-ph.CO].

[18] M. Santos, P. Bull, S. Camera, S. Chen, J. Fonseca, I. Heywood, M. Hilton, M. Jarvis, G. I. G. Jozsa, K. Knowles, L. Leeuw, R. Maartens, E. Malefahlo, K. McAlpine, K. Moodley, P. Patel, A. Pourtsidou, M. Prescott, K. Spekkens, R. Taylor, A. Witzemann, and I. H. Whittam, A Large Sky Survey with MeerKAT, in *MeerKAT Science: On the Pathway to the SKA* (2016) p. 32, arXiv:1709.06099 [astro-ph.CO].

[19] J. Wang, M. G. Santos, P. Bull, K. Grainge, S. Cunningham, J. Fonseca, M. O. Irfan, Y. Li, A. Pourtsidou, P. S. Soares, M. Spinelli, G. Bernardi, and B. Engelbrecht, H I intensity mapping with MeerKAT: calibration pipeline for multidish autocorrelation observations, *MNRAS* **505**, 3698 (2021), arXiv:2011.13789 [astro-ph.CO].

[20] L. B. Newburgh, K. Bandura, M. A. Bucher, T. C. Chang, H. C. Chiang, J. F. Cliche, R. Davé, M. Dobbs, C. Clarkson, K. M. Ganga, T. Gogo, A. Gumba, N. Gupta, M. Hilton, B. Johnstone, A. Karastergiou, M. Kunz, D. Lokhorst, R. Maartens, S. Macpherson, M. Mdlalose, K. Moodley, L. Ngwenya, J. M. Parra, J. Peterson, O. Recnik, B. Saliwanchik, M. G. Santos, J. L. Sievers, O. Smirnov, P. Stronkhorst, R. Taylor, K. Vanderlinde, G. Van Vuuren, A. Weltman, and A. Witzemann, HIRAX: a probe of dark energy and radio transients, in *Proceedings of the SPIE, Volume 9906, id. 99065X 11 pp.* (2016)., Society of Photo-Optical Instrumentation Engineers (SPIE) Conference Series, Vol. 9906 (2016) p. 99065X.

[21] M. Santos, P. Bull, D. Alonso, S. Camera, P. Ferreira, G. Bernardi, R. Maartens, M. Viel, F. Villaescusa-Navarro, F. B. Abdalla, M. Jarvis, R. B. Metcalf, A. Pourtsidou, and L. Wolz, Cosmology from a SKA HI intensity mapping survey, in *Advancing Astrophysics with the Square Kilometre Array (AASKA14)* (2015) p. 19, arXiv:1501.03989 [astro-ph.CO].

[22] T.-C. Chang, U.-L. Pen, K. Bandura, and J. B. Peterson, An intensity map of hydrogen 21-cm emission at redshift $z \sim 0.8$, *Nature (London)* **466**, 463 (2010).

[23] K. W. Masui, E. R. Switzer, N. Banavar, K. Bandura, C. Blake, L. M. Calin, T. C. Chang, X. Chen, Y. C. Li, Y. W. Liao, A. Natarajan, U. L. Pen, J. B. Peterson, J. R. Shaw, and T. C. Voytek, Measurement of 21 cm Brightness Fluctuations at $z \sim 0.8$ in Cross-correlation, *ApJL* **763**, L20 (2013), arXiv:1208.0331 [astro-ph.CO].

[24] L. Wolz, A. Pourtsidou, K. W. Masui, T.-C. Chang, J. E. Bautista, E.-M. Müller, S. Avila, D. Bacon, W. J. Percival, S. Cunningham, C. Anderson, X. Chen, J.-P. Kneib, Y.-C. Li, Y.-W. Liao, U.-L. Pen, J. B. Peterson, G. Rossi, D. P. Schneider, J. Yadav, and G.-B. Zhao, H I constraints from the cross-correlation of eBOSS galaxies and Green Bank Telescope intensity maps, *MNRAS* **510**, 3495 (2022), arXiv:2102.04946 [astro-ph.CO].

[25] C. J. Anderson, N. J. Luciw, Y. C. Li, C. Y. Kuo, J. Yadav, K. W. Masui, T. C. Chang, X. Chen, N. Oppermann, Y. W. Liao, U. L. Pen, D. C. Price, L. Staveley-Smith, E. R. Switzer, P. T. Timbie, and L. Wolz, Low-amplitude clustering in low-redshift 21-cm intensity maps cross-correlated with 2dF galaxy densities, *MNRAS* **476**, 3382 (2018), arXiv:1710.00424 [astro-ph.CO].

[26] S. Cunningham, Y. Li, M. G. Santos, J. Wang, I. P. Carucci, M. O. Irfan, A. Pourtsidou, M. Spinelli, L. Wolz, P. S. Soares, C. Blake, P. Bull, B. Engelbrecht, J. Fonseca, K. Grainge, and Y.-Z. Ma, H I intensity mapping with MeerKAT: power spectrum detection in cross-correlation with WiggleZ galaxies, *MNRAS* **518**, 6262 (2023), arXiv:2206.01579 [astro-ph.CO].

[27] A. Mazumder, L. Wolz, Z. Chen, S. Paul, M. G. Santos, M. Jarvis, J. Townsend, S. Sekhar, and R. Taylor, HI intensity mapping with the MIGHTEE Survey: first results of the HI power spectrum, *MNRAS* **541**, 476 (2025), arXiv:2501.17564 [astro-ph.CO].

[28] T. Di Matteo, R. Perna, T. Abel, and M. J. Rees, Radio Foregrounds for the 21 Centimeter Tomography of the Neutral Intergalactic Medium at High Redshifts, *Astrophys. J.* **564**, 576 (2002), arXiv:astro-ph/0109241 [astro-ph].

[29] S. P. Oh and K. J. Mack, Foregrounds for 21-cm observations of neutral gas at high redshift, *MNRAS* **346**, 871 (2003), arXiv:astro-ph/0302099 [astro-ph].

[30] M. G. Santos, A. Cooray, and L. Knox, Multifrequency Analysis of 21 Centimeter Fluctuations from the Era of Reionization, *Astrophys. J.* **625**, 575 (2005), arXiv:astro-ph/0408515 [astro-ph].

[31] A. de Oliveira-Costa, M. Tegmark, B. M. Gaensler, J. Jonas, T. L. Landecker, and P. Reich, A model of diffuse Galactic radio emission from 10 MHz to 100 GHz, *MNRAS* **388**, 247 (2008), arXiv:0802.1525 [astro-ph].

[32] A. Liu and J. R. Shaw, Data Analysis for Precision 21 cm Cosmology, *Publ. Astron. Soc. Pac.* **132**, 062001 (2020), arXiv:1907.08211 [astro-ph.IM].

[33] A. Liu and M. Tegmark, A method for 21 cm power spectrum estimation in the presence of foregrounds, *Phys. Rev. D* **83**, 103006 (2011), arXiv:1103.0281 [astro-ph.CO].

[34] E. R. Switzer, T.-C. Chang, K. W. Masui, U.-L. Pen, and T. C. Voytek, Interpreting the unresolved intensity of cosmologically redshifted line radiation, *Astrophys. J.* **815**, 51 (2015), arXiv:1504.07527 [astro-ph.CO].

[35] S. Zuo, X. Chen, and Y. Mao, A Semiblind PCA-based Foreground Subtraction Method for 21 cm Intensity Mapping, *Astrophys. J.* **945**, 38 (2023), arXiv:2208.14675 [astro-ph.CO].

[36] E. Chapman, F. B. Abdalla, G. Harker, V. Jelić, P. Labropoulos, S. Zaroubi, M. A. Brentjens, A. G. de Bruyn, and L. V. E. Koopmans, Foreground removal using FASTICA: a showcase of LOFAR-EoR, *MNRAS* **423**, 2518 (2012), arXiv:1201.2190 [astro-ph.CO].

[37] S. Cunningham, M. O. Irfan, I. P. Carucci, A. Pourtsidou, and J. Bobin, 21-cm foregrounds and polarization leakage: cleaning and mitigation strategies, *MNRAS* **504**, 208 (2021), arXiv:2010.02907 [astro-ph.CO].

[38] E. Chapman, F. B. Abdalla, J. Bobin, J. L. Starck, G. Harker, V. Jelić, P. Labropoulos, S. Zaroubi, M. A. Brentjens, A. G. de Bruyn, and L. V. E. Koopmans, The scale of the problem: recovering images of reionization with Generalized Morphological Component Analysis, *MNRAS* **429**, 165 (2013), arXiv:1209.4769 [astro-ph.CO].

[39] L. C. Olivari, M. Remazeilles, and C. Dickinson, Extracting H I cosmological signal with generalized needlet internal linear combination, *MNRAS* **456**, 2749 (2016), arXiv:1509.00742 [astro-ph.CO].

[40] A. Marins, F. B. Abdalla, K. S. F. Fornazier, E. Abdalla, L. H. F. Assis, M. Remazeilles, C. Alexandre Wuensche, L. Barosi, A. R. Queiroz, T. Villela, B. Wang, C. Feng,

R. Landim, V. Liccardo, C. P. Novaes, L. Santos, M. V. dos Santos, and J. Zhang, Foreground removal and 21 cm signal estimates: comparing different blind methods for the BINGO Telescope, *arXiv e-prints* , arXiv:2209.11701 (2022), arXiv:2209.11701 [astro-ph.CO].

[41] N. Kern and A. Liu, Gaussian process foreground subtraction and power spectrum estimation for 21 cm cosmology, *Mon. Not. Roy. Astron. Soc.* **501**, 1463 (2021), arXiv:2010.15892 [astro-ph.CO].

[42] J. R. Shaw, K. Sigurdson, U.-L. Pen, A. Stebbins, and M. Sitwell, All-Sky Interferometry with Spherical Harmonic Transit Telescopes, *Astrophys. J.* **781**, 57 (2014), arXiv:1302.0327 [astro-ph.CO].

[43] A. Ghosh, L. V. E. Koopmans, E. Chapman, and V. Jelić, A Bayesian analysis of redshifted 21-cm H I signal and foregrounds: simulations for LOFAR, *Mon. Not. Roy. Astron. Soc.* **452**, 1587 (2015), arXiv:1506.04982 [astro-ph.CO].

[44] L. Zhang, E. F. Bunn, A. Karakci, A. Korotkov, P. M. Sutter, P. T. Timbie, G. S. Tucker, and B. D. Wandelt, Bayesian Semi-blind Component Separation for Foreground Removal in Interferometric 21 cm Observations, *ApJS* **222**, 3 (2016), arXiv:1505.04146 [astro-ph.CO].

[45] P. H. Sims and J. C. Pober, Joint estimation of the Epoch of Reionization power spectrum and foregrounds, *Mon. Not. Roy. Astron. Soc.* **488**, 2904 (2019), arXiv:1907.02608 [astro-ph.CO].

[46] J. Burba, P. H. Sims, and J. C. Pober, All-sky modelling requirements for Bayesian 21 cm power spectrum estimation with BAYSEOR, *MNRAS* **520**, 4443 (2023), arXiv:2302.04058 [astro-ph.IM].

[47] J. Ding, X. Wang, U.-L. Pen, and X.-D. Li, Correlation-based Beam Calibration of 21 cm Intensity Mapping, *ApJS* **274**, 44 (2024), arXiv:2408.06682 [astro-ph.CO].

[48] J. Asorey, D. Parkinson, F. Shi, Y.-S. Song, K. Ahn, J. Kim, J. Yao, L. Zhang, and S. Zuo, HIR4: cosmology from a simulated neutral hydrogen full sky using Horizon Run 4, *MNRAS* **495**, 1788 (2020), arXiv:2001.00833 [astro-ph.CO].

[49] F. Shi, Y.-S. Song, J. Asorey, D. Parkinson, K. Ahn, J. Yao, L. Zhang, and S. Zuo, HIR4: cosmological signatures imprinted on the cross-correlation between a 21-cm map and galaxy clustering, *MNRAS* **499**, 4613 (2020), arXiv:2006.01407 [astro-ph.CO].

[50] W. Li, H. Xu, Z. Ma, R. Zhu, D. Hu, Z. Zhu, J. Gu, C. Shan, J. Zhu, and X.-P. Wu, Separating the EoR signal with a convolutional denoising autoencoder: a deep-learning-based method, *MNRAS* **485**, 2628 (2019), arXiv:1902.09278 [astro-ph.IM].

[51] T. L. Makinen, L. Lancaster, F. Villaescusa-Navarro, P. Melchior, S. Ho, L. Perreault-Levasseur, and D. N. Spergel, deep21: a deep learning method for 21 cm foreground removal, *JCAP* **2021**, 081 (2021), arXiv:2010.15843 [astro-ph.CO].

[52] S. Gagnon-Hartman, Y. Cui, A. Liu, and S. Ravanbakhsh, Recovering the wedge modes lost to 21-cm foregrounds, *MNRAS* **504**, 4716 (2021), arXiv:2102.08382 [astro-ph.CO].

[53] S. Ni, Y. Li, L.-Y. Gao, and X. Zhang, Eliminating Primary Beam Effect in Foreground Subtraction of Neutral Hydrogen Intensity Mapping Survey with Deep Learning, *Astrophys. J.* **934**, 83 (2022), arXiv:2204.02780 [astro-ph.IM].

[54] J. Kennedy, J. C. Carr, S. Gagnon-Hartman, A. Liu, J. Mirocha, and Y. Cui, Machine-learning recovery of foreground wedge-removed 21-cm light cones for high-z galaxy mapping, *MNRAS* **529**, 3684 (2024), arXiv:2308.09740 [astro-ph.CO].

[55] M. Bianco, S. K. Giri, D. Prelogović, T. Chen, F. G. Mertens, E. Tolley, A. Mesinger, and J.-P. Kneib, Deep learning approach for identification of H II regions during reionization in 21-cm observations - II. Foreground contamination, *MNRAS* **528**, 5212 (2024), arXiv:2304.02661 [astro-ph.IM].

[56] M. Bianco, S. K. Giri, R. Sharma, T. Chen, S. P. Krishna, C. Finlay, V. Nistane, P. Denzel, M. De Santis, and H. Ghorbel, Deep learning approach for identification of H II regions during reionization in 21-cm observations – III. Image recovery, *MNRAS* **541**, 234 (2025), arXiv:2408.16814 [astro-ph.CO].

[57] N. Sabti, R. Purandhar Reddy Sudha, J. B. Muñoz, S. Mishra-Sharma, and T. Youn, A generative modeling approach to reconstructing 21 cm tomographic data, *Machine Learning: Science and Technology* **6**, 015039 (2025), arXiv:2407.21097 [astro-ph.CO].

[58] S.-F. Chen, K.-F. Chen, and C. Dvorkin, Field-level Reconstruction from Foreground-Contaminated 21-cm Maps, *arXiv e-prints* , arXiv:2508.13265 (2025), arXiv:2508.13265 [astro-ph.CO].

[59] D. Alonso, P. G. Ferreira, and M. G. Santos, Fast simulations for intensity mapping experiments, *MNRAS* **444**, 3183 (2014), arXiv:1405.1751 [astro-ph.CO].

[60] C. G. T. Haslam, C. J. Salter, H. Stoffel, and W. E. Wilson, A 408-MHZ All-Sky Continuum Survey. II. The Atlas of Contour Maps, *A&AS* **47**, 1 (1982).

[61] J. Delabrouille, M. Betoule, J. B. Melin, M. A. Miville-Deschénes, J. Gonzalez-Nuevo, M. Le Jeune, G. Castex, G. de Zotti, S. Basak, M. Ashdown, J. Aumont, C. Baccigalupi, A. J. Banday, J. P. Bernard, F. R. Bouchet, D. L. Clements, A. da Silva, C. Dickinson, F. Dodu, K. Dolag, F. Elsner, L. Fauvet, G. Faÿ, G. Giardino, S. Leach, J. Lesgourgues, M. Liguori, J. F. Macías-Pérez, M. Masi, S. Matarrese, P. Mazzotta, L. Montier, S. Mottet, R. Paladini, B. Partridge, R. Piffaretti, G. Prezeau, S. Prunet, S. Ricciardi, M. Roman, B. Schaefer, and L. Toffolatti, The pre-launch Planck Sky Model: a model of sky emission at submillimetre to centimetre wavelengths, *A&A* **553**, A96 (2013), arXiv:1207.3675 [astro-ph.CO].

[62] M. Remazeilles, C. Dickinson, A. J. Banday, M. A. Bigot-Sazy, and T. Ghosh, An improved source-subtracted and destriped 408-MHz all-sky map, *MNRAS* **451**, 4311 (2015), arXiv:1411.3628 [astro-ph.IM].

[63] G. B. Rybicki and A. P. Lightman, *Radiative Processes in Astrophysics* (1986).

[64] K. M. Górski, E. Hivon, A. J. Banday, B. D. Wandelt, F. K. Hansen, M. Reinecke, and M. Bartelmann, HEALPix: A Framework for High-Resolution Discretization and Fast Analysis of Data Distributed on the Sphere, *Astrophys. J.* **622**, 759 (2005), arXiv:astro-ph/0409513 [astro-ph].

[65] S. D. Matshawule, M. Spinelli, M. G. Santos, and S. Ngobese, H I intensity mapping with MeerKAT: primary beam effects on foreground cleaning, *MNRAS* **506**, 5075 (2021), arXiv:2011.10815 [astro-ph.CO].

[66] Y.-S. Song, Y. Zheng, and A. Taruya, Toward a more stringent test of gravity with the redshift space power

spectrum: Simultaneous probe of growth and ampli-

tude of large-scale structure, *PhRvD* **104**, 043528 (2021),
arXiv:2102.01785 [astro-ph.CO].